DOI:
10.1002/mrm.27540

Document Version
Early version, also known as pre-print

Accelerated 3D T_2 Mapping With Dictionary-Based Matching For Prostate Imaging

Elisa Roccia[1], Rohini Vidya Shankar[1], Radhouene Neji[1,2], Gastao Cruz[1], Camila Munoz[1], Rene Botnar[1], Vicky Goh[3], Claudia Prieto[1], and Isabel Dregely[1]

[1] School of Biomedical Engineering and Imaging Sciences, King's College London, London, United Kingdom

[2] Siemens Healthcare Limited, Frimley, United Kingdom

[3] Cancer Imaging, King's College London, London, United Kingdom

Short Title: Accelerated 3D T_2 mapping of the prostate

Submitted as Full Paper to Magnetic Resonance in Medicine

Word count: 4086

Corresponding author:

Elisa Roccia

Department of Biomedical Engineering, 3rd floor Lambeth Wing

St Thomas' Hospital, Westminster Bridge Road, London SE1 7EH, United Kingdom

Email: elisa.roccia@kcl.ac.uk

ABSTRACT

Purpose: To develop a fast and accurate method for 3D T_2 mapping of prostate cancer using undersampled acquisition and dictionary-based fitting.

Methods: 3D high-resolution T_2-weighted images (0.9 x 0.9 x 3 mm^3) were obtained with a multi-shot T_2-prepared bSSFP acquisition sequence (T_2prep-bSSFP) using a prospectively undersampled 3D variable density Cartesian trajectory. Each T_2-weighted image was reconstructed using Total Variation regularized SENSE. A flexible simulation framework based on extended phase graphs generated a dictionary of magnetization signals, which was customized to the proposed sequence. The dictionary was matched to the acquired T_2-weighted images to retrieve T_2 values, which were then compared to gold standard spin echo acquisition values using monoexponential fitting. The proposed approach was validated in simulations and a T2 phantom, and feasibility was tested in healthy subjects.

Results: The simulation analyses showed that the proposed T_2 mapping approach is robust to noise and insensitive to observed T_1 variations. Compared to gold standard, T_2 values obtained in the phantom with T_2prep-bSSFP using monoexponential fitting were significantly different ($P < 0.05$), whereas the acquisition-specific dictionary-based matching corrected for these inaccurate estimates. T_2 values obtained in the phantom with the accelerated acquisition matched those obtained with the fully sampled acquisition ($r = 0.99$). T_2 values estimated in the peripheral zone, central gland and muscle of the young healthy subjects were 97 ± 14 ms, 76 ± 7 ms and 36 ± 3 ms respectively.

Conclusion: 3D quantitative high-resolution T_2 mapping of the whole prostate can be achieved in 3 min with improved accuracy compared to the reference standard.

Key words: prostate cancer imaging; quantitative MRI; T_2 mapping; 3T MRI

INTRODUCTION

Prostate cancer (PCa) is one of the most frequent types of cancer in men, with 1.1 million diagnoses worldwide in 2012 (1). The incidence of PCa varies greatly, with an increased mortality rate in less developed countries and in black populations (1). The standard clinical routine for its diagnosis consists of the measurement of serum prostate-specific antigen, digital rectal examination and transrectal ultrasound-guided biopsy. However, this algorithm may not accurately detect cancer or assess its aggressiveness. Many cases of clinically significant cancers are missed and overtreatment of low-risk PCa and underuse of active surveillance in this patient group remains a significant clinical challenge (2,3).

Multiparametric magnetic resonance imaging (mpMRI) of the prostate, which consists of the acquisition of 2D T_2-weighted (T_2w), diffusion-weighted and gadolinium-based dynamic contrast-enhanced images, has shown great potential for detecting PCa, facilitated by consensus guidelines for acquisition, analysis and reporting (PIRADS) (4,5), and has been shown to correlate with pathologic Gleason score (2,3). In particular, high-resolution T_2w imaging depicts prostate anatomy and has the ability to detect and characterize lesions, particularly within the transitional zone where it is the primary image contrast for PIRADS scoring (5), with cancerous lesions appearing of intermediate signal intensity on T_2w-MRI. Even though the current literature reports that sensitivity for PCa detection and diagnosis is high (range of sensitivity values reported: 58 – 95%) (4,6,7), the diagnostic ability of mpMRI for PCa strongly varies. 2D T_2w images are evaluated in a qualitative manner and thus diagnosis highly depends on reader experience, sequence parameters and MRI scanner, geometry (transversal vs. sagittal vs. coronal), image quality and institutional standards. Low specificity has been reported in the detection of clinically significant cancers (4), and low sensitivity in the detection of small, intermediate

grade lesions, and cancers located in the apex (7).

Quantitative 3D MRI directly relates to the underlying tissue characteristics and may provide more accurate and reproducible information than qualitative assessment, which can improve diagnostic ability, particularly in follow-up (active surveillance) and longitudinal studies (8). In particular, quantitative mapping of T_2 relaxation rate has already shown promising results for PCa discrimination (9–11). Low T_2 values were found to correlate well with the low citrate levels of cancerous tissue, which is characterized by low acinar structure (12). Nevertheless, quantitative T_2 mapping is not yet standard in clinical routine because of the long scan times required for the acquisition of multiple T_2 contrasts (5). Therefore, the clinical challenge is the development of an accurate and robust method for quantitative T_2 mapping, with 3D coverage, high resolution and signal-to-noise ratio (SNR), which can be performed in clinically acceptable scan times.

The reference standard T_2 mapping approach consists of a 2D multi-contrast scan in which several spin-echo (SE) images are acquired at different echo times (TE) and are then fitted pixel wise to a monoexponential function that models the T_2 decay (8,9). As the SE acquisition has prohibitively long scan times and is prone to motion artifacts due to peristalsis or physiological bulk motion, several undersampled reconstruction approaches have been proposed to enable T_2 mapping in feasible scan times (9,13–18). A turbo spin-echo (TSE) acquisition can be used to reduce scan times by echo train sampling. However, the length of the echo train (“turbo factor”), and thus the scan time reduction, is associated with increased image blurring. To acquire multi-contrast T_2w images for quantitative T_2 mapping, the scan time may still be too long. Thus, the acquisition is typically limited to 2D. Furthermore, the contribution of stimulated echoes in the TSE echo train results in a deviation of the signal from the assumption of monoexponential behavior and hence leads to inaccurate estimates (19).

Improved accuracy in T_2 quantification can be achieved using simulation-based

methods rather than the standard oversimplified monoexponential fit. These methods are characterized by more complex but accurate modeling of the acquisition pulse sequence effects on the magnetization. To retrieve quantitative T_2 values in each voxel, a matching process is performed between the measured signal and a dictionary (database) of magnetization signals, which are generated using either Bloch or extended phase graphs (20) (EPG) simulations (21,18).

Alternative acquisition sequences for T_2 mapping have been investigated such as Carr-Purcell-Meiboom-Gill sequence (10), double-echo steady-state (DESS) (22), and triple echo steady-state (23). The balanced steady-state free precession (bSSFP) sequence has been often used to perform segmented acquisitions interleaved with magnetization preparation, with promising results in T_2 quantitative parametric mapping in both cardiac (24–29) and prostate (30–32) applications. Magnetization preparation sequences are advantageous because of the flexibility to add the preparation of multiple contrasts, such as T_1-preparation (33), T_2-preparation (T_2prep) (34,35), fat saturation, and combinations of these (24).

In this study, we sought to develop accurate and fast 3D T_2 mapping of the whole prostate. We propose the use of an accelerated 3D multi-shot T_2prep-bSSFP acquisition sequence, combined with a Cartesian Acquisition with Spiral PRofile order (CASPR) (36) trajectory. This trajectory is advantageous as it is Cartesian, and therefore does not require computationally demanding gridding steps in the reconstruction, it is centric in k_y-k_z thus enabling the immediate encoding of the contrast generated by the magnetization preparation pre-pulses, and is suitable for undersampling to reduce scan time. For T_2 mapping, we use a dictionary-based T_2 mapping method that is customized to the acquisition sequence and specified imaging parameters. First, the dictionary-based T_2 mapping method is validated in both simulations and a standardized-T_1/T_2 phantom

experiment. Then, the undersampled acquisition is validated in the phantom, and a feasibility study is performed on healthy subjects.

METHODS

The 3D high-resolution data were acquired using a prototype segmented multi-shot T_2prep-bSSFP sequence (shot length = TR), each preceded by an adiabatic T_2prep module (34,35) with different durations, and 14 ramp-up pulses for magnetization stabilization. In each shot a fixed number of samples, so called segments, were acquired and assigned to unique k_y-k_z positions. The bSSFP readout used a 3D CASPR trajectory (36). This trajectory was prospectively undersampled using a variable density (VD) undersampling scheme, with a fully sampled center region of the k-space and an undersampled periphery (Figure 1A). The variable density data was reconstructed with Total Variation regularized SENSE (TV-SENSE) reconstruction (37,38).

A simulation framework based on the EPG formalism (20) was implemented in MATLAB (Mathworks, Natick, MA). This framework enabled evaluation of the acquisition-specific magnetization evolution and was used to: 1) optimize the T_2prep-bSSFP sequence parameters for maximum SNR and tissue contrast, while keeping acquisition time short, 2) characterize the dependencies of the acquisition scheme on T_1 and flip angle (FA), and 3) implement the dictionary-based T_2 matching.

The multi-dimensional dictionary of signals was generated such that each dictionary entry reflects the signal evolution as a function of a given tissue type (with specific intrinsic parameters T_1, T_2 relaxation rate) and fixed extrinsic (T_2prep-bSSFP imaging sequence specific) parameters. Each dictionary entry was calculated as the average over the first readout segment in each shot, so as to reflect encoding of the contrast information in the centric trajectory acquisition (Figure 1). The range of relaxation times simulated was T_1 = [1200, …, 2300] ms (steps of 10 ms) and T_2 = [20, …, 250] ms (steps of 1 ms), which represent typical prostate tissue values.

In order to determine the quantitative T_2 values, matching was performed for each image voxel by minimizing the L_2-norm of the differences between the normalized experimental data and the precomputed dictionary of simulated signals, with an exhaustive search over all dictionary entries. The dictionary-based T_2 matching can be performed either with a fixed T_1 value or with a voxel-specific T_1, which requires the separate acquisition and incorporation of a T_1 map into the matching algorithm.

A phantom experiment was performed to validate the proposed dictionary-based T_2 mapping technique and the undersampled VD acquisition. Feasibility for prostate T_2 mapping was then tested in healthy subjects, following approval by the local institutional review board and informed consent. Both phantom and in-vivo experiments were performed on a 3T PET-MR scanner (Biograph mMR, Siemens Healthcare, Erlangen, Germany), using MR-only capability. Before image acquisition, simulations were performed to investigate on the magnetization signal dependence on T_1 and FA, and on the robustness to noise of the dictionary-based T_2 mapping in comparison with monoexponential fitting.

Simulations

T_1 and FA dependence

To characterize potential confounding influences on T_2 estimates by (unknown) T_1 and FA variations, the simulated signal intensity was analyzed as a function of T_1 and FA for a range of T_2 values. A further simulation was performed to assess the impact on the T_2 estimated using the proposed approach if a globally fixed (rather than voxel-based measured) T_1 was used, and if this introduces a bias in the T_2 estimation. Four different dictionary entries were simulated representing different tissue types, for all combinations of low T_1^{true} = 1700 ms, high T_1^{true} = 2200 ms, low T_2^{true} = 50 ms, high T_2^{true} = 150 ms, with

the T_2 values chosen to represent cancerous and healthy tissue as an average of typically reported T_2 values (9,39,40). Each of these dictionary entries was then matched to the dictionary assuming a globally fixed T_1 different from the T_1^{true} to characterize deviations of T_2 estimates as a function of T_1 variations.

SNR analysis

Monte Carlo simulations were performed to evaluate the robustness to noise of the proposed approach, comparing this with the reference monoexponential fitting. Different levels of random white Gaussian noise (SNR = 10, 20, 30, 40, 50, 80, 100) were added to the simulated transverse magnetization, T_2 matching was performed, and this was repeated 5000 times. Accuracy and precision were then calculated as the mean and standard deviation of T_2 estimated over the 5000 repetitions, respectively. This SNR analysis was performed for two dictionary entries corresponding to different prostate tissue types: T_1 = 2200 ms (41) and $T_2^{low/high}$ = 50/150 ms. This SNR analysis was performed by estimating the T_2 value using the dictionary matching with six different T_2prep (T_2prep duration: 0, 45, 70, 90, 120, 150 ms), with only three T_2prep (T_2prep duration: 0, 90, 150 ms), and also by using a simplified monoexponential fitting for comparison with the proposed dictionary-based matching.

Phantom

Acquisition

The standardized T_1/T_2 phantom used to test the proposed T_2 mapping method contained 9 tubes each with different T_1 and T_2 relaxation times (42). Imaging parameters of the proposed prototype 3D T_2prep-bSSFP sequence were chosen consistently with the EPG-guided sequence optimization, ensuring that the total acquisition time is minimized while maintaining SNR and contrast: shot length TR = 1600 ms, flip angle FA = 57°, number of

bSSFP segments in each shot Nseg = 96. Other imaging parameters were: transversal orientation, matrix size 304 x 304 x 32, resolution 0.9 x 0.9 x 3 mm^3, and bSSFP-TR/TE = 4.0/2.0 ms. For T_2 mapping, three T_2prep-bSSFP images with different T_2prep durations (0, 90, 150 ms) were acquired sequentially, both fully sampled (FS) and VD. The choice of using only three T_2prep was based on the simulation results, and on an additional experiment performed on the phantom which showed that the T_2 estimated with dictionary matching using three T_2prep was highly correlated with values obtained using six T_2prep (Supplementary Figure 1). The acquisition time was TA = 2 min 40 s for a fully sampled (FS) acquisition (100 shots) and 1 min for a VD factor of 3 (37 shots). For reference T_2 mapping, 2D SE images with long TR (TR = 10 s) to allow for full magnetization recovery were also acquired, with TE matched to the three different T_2prep durations. This was a single slice acquisition that matched the central slice of the 3D T_2prep-bSSFP. Acquisition parameters for 2D SE were: 256 x 256 matrix size, transversal orientation, 0.85 x 0.85 mm^2 resolution, TR = 10 s, TE = 12, 90, 150 ms, TA = 38 min 37 s for each T_2w image (total TA = 1 h 55 min 51 s). An inversion recovery-SE (IR-SE) T_1 map was also acquired with 256 x 256 matrix, transversal orientation, 0.85 x 0.85 mm^2 resolution, TR = 10 s, TE = 12 ms, TI = 50, 100, 150, 300, 500, 1000, 2000, 4000, 6000 ms, TA = 42 min 52 s for each T_1w image (total TA = 6 h 25 min 48 s).

Data analysis

The two sets (FS and VD) of three 3D T_2prep-bSSFP T_2w images were fitted to obtain quantitative T_2 in two ways: i) using a monoexponential model (which does not take into account incomplete magnetization recovery for a TR = 1600 ms), and ii) using the proposed approach with EPG-based dictionary matching. The reference standard SE T_2 map was obtained with a standard monoexponential fit. The IR-SE T_1 map was included in the matching algorithm to account for the significant variation of T_1 values of the different

tubes. Regions of interest (ROIs) were drawn in the central slice of the 3D acquisition, which corresponds to the single slice of the 2D acquisition, for each phantom tube, and the T_2 estimates are presented as mean ROI value ± standard deviation (STD). Particular focus was given to four phantom tubes characterized by different combinations of T_1 and T_2 relaxation times: low T_1 and T_2 (LL), low T_1 and high T_2 (LH), high T_1 and low T_2 (HL), and high T_1 and T_2 (HH).

The following comparisons were performed:

1. $SE^{monoexponential}$ vs T_2prep-bSSFP$_{FS}^{monoexponential}$ vs T_2prep-bSSFP$_{FS}^{dictionary}$: T_2 values obtained with reference 2D SE using monoexponential fit vs FS 3D T_2prep-bSSFP using monoexponential fit vs FS 3D T_2prep-bSSFP using dictionary based-matching

2. T_2prep-bSSFP$_{FS}^{dictionary}$ vs T_2prep-BSSFP$_{VD}^{dictionary}$: T_2 values obtained with FS vs VD 3D T_2prep-bSSFP, both using dictionary-based matching
3. $SE^{monoexponential}$ vs T_2prep-bSSFP$_{VD}^{dictionary}$: finally, this compared the reference standard single echo SE method (total TA = 1:55:51 hours) with the proposed VD T_2prep-bSSFP method that requires only 3 min.

The results were compared using regression analysis and Pearson's correlation coefficient (r); statistical difference was tested using a paired-sample *t* test with threshold P = 0.05.

Healthy subjects

Acquisition

The feasibility study included eight healthy male subjects, age 26 ± 6 years. The in-vivo VD 3D T_2prep-bSSFP acquisition parameters matched the phantom acquisition parameters: TR = 1600 ms, FA = 57°, Nseg = 96, transversal orientation, matrix size 304

x 304 x 32, resolution 0.9 x 0.9 x 3 mm^3, bSSFP-TR/TE = 4.0/2.0 ms, T_2prep durations (0, 90, 150 ms) acquired sequentially. To compare image quality, a clinical standard transverse 2D T2w TSE image was acquired for all eight subjects (320 x 256 matrix, 0.6 x 0.8 x 3 mm^3 resolution, TR/TE = 6470/89 ms, FA = 150°, TA = 2 min 16 s), an example image shown in **Error! Reference source not found.**.

Data analysis

The proposed dictionary-based T_2 mapping method with VD T_2prep-bSSFP was applied to the whole healthy volunteer population. Based on our simulation results, a T_1 map was not included in the matching algorithm, but a fixed T_1 value of 2200 ms (41) (representative of prostate T_1) was used instead. In all subjects, quantitative analysis of T_2 values was performed in three different ROIs: prostate peripheral zone (PZ), prostate central gland (CG), and muscle; the results are presented as mean ± STD using boxplots.

RESULTS

Simulations

The EPG-simulated magnetization evolution in time for the proposed acquisition scheme is shown in Figure 1B for two simulated prostate tissue types: cancerous (T_2 = 50 ms) and healthy (T_2 = 150 ms).

T_1 and FA dependence

The dependences of the magnetization signal extracted from the simulated dictionary on T_1 and FA are shown in Figure 2. While the signal intensity was more than a factor of 2.5 different for T_2 = 50 ms vs T_2 = 150 ms, which underlines the desired T_2 sensitivity of the proposed scheme, the signal intensity experienced only slight variations over a range of T_1 typically observed in the prostate (Figure 2A) and FA (Figure 2B), demonstrating insensitivity to both these parameters. The maximum signal variation was observed for the highest T_2 value (150 ms), with an absolute signal change of -9.5% between T_1 = 1200 ms and 2300 ms, and of 13.9% between FA = 40^o and 90^o.

In addition to this, the simulations showed that the dictionary-based matching is robust to T_1 variations when T_2^{true} = 50 ms, for both T_1^{true} = 1700 and 2200 ms (light blue curves in Figure 3A and 3B), over a wide range of (wrongly) assumed T_1 values (1500-2400 ms). For T_2^{true} = 150 ms (dark blue curves in Figure 3A and 3B) the T_2 estimates experienced slight under- and overestimation when the (wrongly) assumed T_1 was respectively lower and higher than T_1^{true} (maximum absolute bias: 0.03% when T_1^{true} = 1700, 0.02% when T_1^{true} = 2200).

SNR analysis

The SNR analysis results are presented in Figure 4. For illustration, Figure 4A shows a dictionary entry with the corresponding 100 noisy signals overlapped as an example case of SNR analysis for SNR = 10. Figure 4B summarizes the SNR analysis simulation, showing accuracy and precision for the two tissues ($T_2^{low/high}$ = 50/150 ms, both with T_1 = 2200 ms), for all the T_2 mapping methods under investigation. The monoexponential fit led to the lowest accuracy among all the scenarios analyzed, with a bias of 19.7 ms (T_2^{true} – $T_2^{estimated}$) and precision of 21 ms (STD) in the most challenging case of T_2^{high} at the lowest SNR. The accuracy increased when using the dictionary-based T_2 matching, with very similar results when using six or three T_2prep. In particular, the proposed method using only three T_2prep modules led to a maximum bias of -0.4 ms in the T_2^{high} case at the lowest SNR, and a STD of 15.4 ms. For a more realistic SNR level (SNR = 30) the proposed T_2 mapping approach showed a maximum bias of -0.01 and -0.16 ms for the T_2^{low} and T_2^{high} case respectively, and a corresponding STD of 1.99 and 5.04 ms. Overall, as expected, accuracy and precision increased at higher SNR and lower T_2 values.

Phantom

The results of the phantom T_2 mapping are shown in Figure 5. Figure 5B shows the comparison of the T_2 estimates obtained with the FS 3D T_2prep-bSSFP using both monoexponential fit and dictionary-based matching compared with the gold-standard 2D SE using monoexponential fit. This analysis was performed for the four tubes highlighted in Figure 5A, so as to represent different combinations of T_1 and T_2 values, as previously detailed. In concordance with our simulation results, the phantom data confirmed that the use of the monoexponential fit with the T_2prep-bSSFP provided T_2 estimates that are significantly different ($P < 0.05$) from those obtained with the SE approach, whereas the T_2 values obtained with the dictionary approach were highly correlated (correlation of r =

0.99) with the reference SE values (Figure 5B). The tube with the highest T_1 and T_2 values (HH) was characterized by the lowest accuracy and precision. Results obtained with the VD T_2prep-bSSFP were highly correlated with the FS acquisition results for all phantom tubes (r = 0.99, Figure 5C). The use of the three-fold accelerated acquisition resulted in a scan time reduction from a TA = 8:03 min (100 shots per 3D acquisition x three T_2prep) to TA = 3 min (37 shots per 3D acquisition x three T2prep). Figure 5D shows the final comparison between the gold standard 2D SE using monoexponential fit (TA = 1 h 55 min 51 s) and the proposed 3D VD T_2prep-bSSFP dictionary-based matching using three T_2prep (TA = 3 min), which were highly correlated (r = 0.99) over a range of T_1 and T_2 values.

Healthy subjects

T_2w images obtained with the VD 3D T_2prep-bSSFP sequence at different T_2prep durations and the corresponding dictionary-based T_2map are shown in Figure 6 for three healthy subjects. T_2 estimates obtained with the proposed VD T_2prep-bSSFP sequence in the PZ, CG and muscle for all healthy subjects are reported in Figure 8A. The T_2 map obtained with the proposed approach for the oldest subject in the cohort (age 37), representing the only outlier in the T_2 estimates, is shown in Figure 8B. An example case of a healthy subject with increased T_2 due to focal inflammation is presented in Figure 9.

DISCUSSION

We have demonstrated the feasibility of using an accelerated 3D T_2-prepared multi-shot-bSSFP sequence combined with a dictionary-based matching method to rapidly quantify T_2 values in the prostate. The proposed method enabled the acquisition of a 3D T_2w image set of the full pelvis FOV at 0.9 x 0.9 x 3 mm^3 resolution in only 1 min, similar to that obtained in (22) with a DESS sequence. The advantage of the proposed segmented acquisition in combination with dictionary based simulation of the acquisition specific magnetization evolution lies in its flexibility to incorporate other magnetization preparation modules, e.g. diffusion preparation, T_1 preparation, fat suppression, and/or motion correction. Interleaved acquisitions, where multiple MR contrasts could be generated at each segment of the sequence, provide the prospect of a mpMRI approach that would enable a full tissue characterization with multiple and inherently co-registered quantitative maps in a single acquisition.

Our findings on the SNR analysis showed robustness of the proposed approach to different noise levels, with results comparable to that obtained in other studies (18). The analysis on T_1 variation effects showed that small T_1 variations (in the range of T_1 values typically found within the prostate) do not affect the T_2 estimate significantly, providing the rationale for using a fixed T_1 value in our in-vivo study.

The main strength of simulation-based T_2 mapping is that it accounts for the magnetization evolution specific for the chosen acquisition sequence that cannot be accounted for when using the oversimplified monoexponential model, for example the incomplete T_1 recovery in the rapid multi-shot acquisition (TR = 1600 ms, T_1 of the prostate ~ 2000 ms). Our findings in simulations and phantom experiments consistently showed that acquisition-specific dictionary-based matching was able to obtain accurate T_2 estimates, while those obtained with the standard monoexponential fit showed significant deviation.

In the phantom study, we could acquire a long (TA = 1 h 55 min 51 s) SE sequence as true gold standard to evaluate bias and precision of our method. However, there is no gold standard for T_2 mapping in prostate imaging, indeed different studies have used different reference methods for comparison with their proposed approach, demonstrating a lack of standardization in prostate T_2 mapping.

Our in-vivo T_2 values were lower than typical prostate T_2 values reported in the literature (9,22,43) which is likely due to the young age of our study population (26 ± 6). This assumption is supported by measurements of T2 in muscle with our sequence which was in agreement with values reported in literature (22).

One limitation of this study is the presence of banding artifacts in the T_2w images due to the use of a bSSFP readout. However, the prostate area was not affected by these artifacts and, if present, they were mainly seen in the region of fat. While bSSFP yields the highest SNR efficiency, alternative methods with no or little banding artifacts include the non fully-balanced (SSFP, DESS) or spoiled (GRE, FLASH) readout acquisition, which could be used instead.

Future work includes modifying this prototype sequence for acquiring diffusion prepared images, retrieving apparent diffusion coefficient (ADC) maps, and then combined T_2 / ADC maps by exploiting the developed EPG-based simulation framework. Furthermore, the in-vivo work will be extended to include healthy subjects with an age closer to the average age of PCa patients.

CONCLUSION

We have shown that rapid 3D T_2-mapping of the prostate is feasible in 3 min using on an accelerated 3D multi shot T_2-prepared acquisition combined with a dictionary-based T_2 mapping reconstruction. Our proposed approach showed high precision and accuracy for T_2 quantification and allows for a flexible incorporation of additional magnetization preparation modules to be used in a mpMRI protocol for PCa detection and characterization.

References

1. WHO. GLOBOCAN 2012: Estimated Incidence, Mortality and Prevalence Worldwide in 2012 [Internet]. 2012 [cited 2018 Mar 15]. Available from: http://globocan.iarc.fr/Pages/fact_sheets_cancer.aspx
2. Hegde J V., Mulkern R V., Panych LP, Fennessy FM, Fedorov A, Maier SE, et al. Multiparametric MRI of prostate cancer: An update on state-of-the-art techniques and their performance in detecting and localizing prostate cancer. J Magn Reson Imaging. 2013;37(5):1035–54.
3. Barentsz JO, Richenberg J, Clements R, Choyke P, Verma S, Villeirs G, et al. ESUR prostate MR guidelines 2012. Eur Radiol. 2012;22(4):746–57.
4. Ahmed HU, El-Shater Bosaily A, Brown LC, Gabe R, Kaplan R, Parmar MK, et al. Diagnostic accuracy of multi-parametric MRI and TRUS biopsy in prostate cancer (PROMIS): a paired validating confirmatory study. Lancet [Internet]. The Author(s). Published by Elsevier Ltd. This is an Open Access article under the CC BY license; 2017;6736(16):1–8. Available from: http://linkinghub.elsevier.com/retrieve/pii/S0140673616324011
5. Weinreb JC, Barentsz JO, Choyke PL, Cornud F, Haider MA, Macura KJ, et al. PI-RADS Prostate Imaging - Reporting and Data System: 2015, Version 2. Eur Urol [Internet]. European Association of Urology; 2016;69(1):16–40. Available from: http://dx.doi.org/10.1016/j.eururo.2015.08.052
6. Isebaert S, Van Den Bergh L, Haustermans K, Joniau S, Lerut E, De Wever L, et al. Multiparametric MRI for prostate cancer localization in correlation to whole-mount histopathology. J Magn Reson Imaging. 2013;37(6):1392–401.
7. Le JD, Tan N, Shkolyar E, Lu DY, Kwan L, Marks LS, et al. Multifocality and prostate cancer detection by multiparametric magnetic resonance imaging: Correlation with whole-mount histopathology. Eur Urol [Internet]. European Association of Urology; 2015;67(3):569–76. Available from: http://dx.doi.org/10.1016/j.eururo.2014.08.079
8. Liu W, Turkbey B, Senegas J, Remmele S, Xu S, Kruecker J, et al. Accelerated T2 mapping for characterization of prostate cancer. Magn Reson Med. 2011;65(5):1400–6.
9. Yamauchi FI, Penzkofer T, Fedorov A, Fennessy FM, Chu R, Maier SE, et al. Prostate Cancer Discrimination in the Peripheral Zone With a Reduced Field-of-View T2 -mapping MRI Sequence. Magn Reson Imaging. 2015;33(5):525–30.
10. Roebuck JR, Haker SJ, Mitsouras D, Rybicki FJ, Tempany CM, Mulkern R V. Carr-Purcell-Meiboom-Gill (CPMG) Imaging of Prostate Cancer: Quantitative T2 Values for Cancer Discrimination. Magn Reson Imaging. 2009;27(4):497–502.
11. van Houdt PJ, Agarwal HK, van Buuren LD, Heijmink SWTPJ, Haack S, van der Poel HG, et al. Performance of a fast and high-resolution multi-echo spin-echo sequence for prostate T2 mapping across multiple systems. Magn Reson Med [Internet]. 2017;0(January):1–9. Available from: http://doi.wiley.com/10.1002/mrm.26816%5Cnhttp://www.ncbi.nlm.nih.gov/pubmed/28671331
12. Liney GP, Turnbull LW, Lowry M, Turnbull LS, Knowles AJ, Horsman A. In vivo quantification of citrate concentration and water T2 relaxation time of the pathologic prostate gland using H1 MRS and MRI. Magn Reson Imaging. 1997;15(10):1177–86.

13. Agarwal HK, Senegas J, Turkbey B, Bernardo M, Nielsen T, Kcupp J, et al. Whole-Prostate T2 mapping in under 6 minutes using autocalibration and partial-fourier MRI. Proc Intl Soc Mag Reson Med. 2012;20:2401.
14. Lee D, Jin KH, Kim EY, Park SH, Ye JC. Acceleration of MR parameter mapping using annihilating filter-based low rank hankel matrix (ALOHA). Magn Reson Med. 2016;76(6):1848–64.
15. Zhao B, Wenmiao L, Hitchens K, Lam F, Ho C, Liang Z-P. Accelerated MR Parameter Mapping with Low-Rank and Sparsity Constraints. Magn Reson Med. 2015;489–98.
16. Peng X, Ying L, Liu Y, Yuan J, Liu X, Liang D. Accelerated exponential parameterization of T2 relaxation with model-driven low rank and sparsity priors (MORASA). Magn Reson Med. 2016;0(November 2015).
17. Doneva M, Boernert P, Eggers H, Stehning C, S??n??gas J, Mertins A. Compressed sensing reconstruction for magnetic resonance parameter mapping. Magn Reson Med. 2010;64(4):1114–20.
18. Ben-Eliezer N, Sodickson DK, Block KT. Rapid and accurate T2 mapping from multi-spin-echo data using bloch-simulation-based reconstruction. Magn Reson Med. 2015;73(2):809–17.
19. Hennig J. Multiecho imaging sequences with low refocusing flip angles. J Magn Reson. 1988;78(3):397–407.
20. Weigel M. Extended phase graphs: Dephasing, RF pulses, and echoes - Pure and simple. J Magn Reson Imaging. 2015;41(2):266–95.
21. Stöcker T, Keil F, Vahedipour K, Brenner D, Pracht E, Shah NJ. MR parameter quantification with magnetization-prepared double echo steady-state (MP-DESS). Magn Reson Med. 2014;72(1):103–11.
22. Dregely I, Margolis DAJ, Sung K, Zhou Z, Rangwala N, Raman SS, et al. Rapid quantitative T2 mapping of the prostate using three-dimensional dual echo steady state MRI at 3T. Magn Reson Med. 2016;76(6):1720–9.
23. Heule R, Ganter C, Bieri O. Triple echo steady-state (TESS) relaxometry. Magn Reson Med. 2014;71(1):230–7.
24. Akcakaya M, Weingartner S, Basha TA, Roujol S, Bellm S, Nezafat R. Joint myocardial T1 and T2 mapping using a combination of saturation recovery and T2-preparation. Magn Reson Med. 2016;76(3):888–96.
25. Aliotta E, Moulin K, Zhang Z, Ennis DB. Simultaneous measurement of T 2 and apparent diffusion coefficient (T 2 +ADC) in the heart with motion-compensated spin echo diffusion-weighted imaging. Magn Reson Med [Internet]. 2017;0(March):1–9. Available from: http://doi.wiley.com/10.1002/mrm.26705
26. Santini F, Kawel-Boehm N, Greiser A, Bremerich J, Bieri O. Simultaneous T1 and T2 quantification of the myocardium using cardiac balanced-SSFP inversion recovery with interleaved sampling acquisition (CABIRIA). Magn Reson Med. 2015;74(2):365–71.
27. Giri S, Chung Y-C, Merchant A, Mihai G, Rajagopalan S, Raman S V, et al. T2 quantification for improved detection of myocardial edema. J Cardiovasc Magn Reson [Internet]. 2009;11(1):56. Available from: http://jcmr-online.biomedcentral.com/articles/10.1186/1532-429X-11-56
28. Van Heeswijk RB, Feliciano H, Bongard C, Bonanno G, Coppo S, Lauriers N, et al. Free-breathing 3 T magnetic resonance T2-mapping of the heart. JACC Cardiovasc Imaging [Internet]. Elsevier Inc.; 2012;5(12):1231–9. Available from: http://dx.doi.org/10.1016/j.jcmg.2012.06.010
29. Tourais J, Henningsson M, Botnar R. Free-breathing 3D myocardial T2 mapping using image-based respiratory motion correction. International Society for

Magnetic Resonance in Medicine (ISMRM). 2016.
30. Nguyen C, Sharif-Afshar AR, Fan Z, Xie Y, Wilson S, Bi X, et al. 3D high-resolution diffusion-weighted MRI at 3T: Preliminary application in prostate cancer patients undergoing active surveillance protocol for low-risk prostate cancer. Magn Reson Med. 2016;75(2):616–26.
31. Dregely I, Prieto C, Neji R, Munoz C, Botnar R, Mallia A, et al. " Push-button " PET / MRI using a continuous scan 3D quantitative T2 MRI sequence. Proc Intl Soc Mag Reson Med. 2017;1239:2078.
32. Shankar R, Cruz G, Neji R, Goh V, Botnar RM, Prieto C, et al. Accelerated 3D T2-Mapping of the Prostate in 3.5 min using TV-SENSE Reconstruction. ESMRMB. 2017. p. 139.
33. Kellman P, Hansen MS. T1-mapping in the heart: Accuracy and precision. J Cardiovasc Magn Reson. 2014;16(1):1–20.
34. Brittain JH, Hu BS, Wright GA, Meyer CH, Macovski A, Nishimura DG. Coronary Angiography with Magnetization-PreparedT2 Contrast. Magn Reson Med [Internet]. 1995;33(5):689–96. Available from: http://doi.wiley.com/10.1002/mrm.1910330515
35. Botnar RM, Stuber M, Danias PG, Kissinger K V, Manning WJ. Improved Coronary Artery Definition With T2-Weighted, Free-Breathing, Three-Dimensional Coronary MRA. Circulation [Internet]. 1999;99(24):3139–48. Available from: http://circ.ahajournals.org/content/99/24/3139.abstract
36. Prieto C, Doneva M, Usman M, Henningsson M, Greil G, Schaeffter T, et al. Highly efficient respiratory motion compensated free-breathing coronary MRA using golden-step Cartesian acquisition. J Magn Reson Imaging. 2015;41(3):738–46.
37. Cruz G, Atkinson D, Buerger C, Schaeffter T, Prieto C. Accelerated motion corrected three-dimensional abdominal MRI using total variation regularized SENSE reconstruction. Magn Reson Med. 2016;75(4):1484–98.
38. Lustig M, Donoho DL, Santos JM, Pauly JM. Compressed sensing MRI. IEEE Signal Process Mag [Internet]. 2008;25(March 2008):72–82. Available from: http://ieeexplore.ieee.org/xpls/abs_all.jsp?arnumber=4472246
39. Gibbs P, Liney GP, Pickles MD, Zelhof B, Rodrigues G, Turnbull LW. Correlation of ADC and T2 measurements with cell density in prostate cancer at 3.0 Tesla. Invest Radiol [Internet]. 2009;44(9):572–6. Available from: http://www.ncbi.nlm.nih.gov/pubmed/19692841
40. Sabouri S, Chang SD, Savdie R, Zhang J, Jones EC, Goldenberg SL, et al. Luminal Water Imaging: A New MR Imaging T2 Mapping Technique for Prostate Cancer Diagnosis. Radiology [Internet]. 2017;284(2):161687. Available from: http://pubs.rsna.org/doi/10.1148/radiol.2017161687
41. Rangwala NA, Dregely I, Wu HH, Sung K. Optimization and evaluation of reference region variable flip angle (RR-VFA) B1+ and T1Mapping in the Prostate at 3T. J Magn Reson Imaging. 2017;45(3):751–60.
42. Captur G, Gatehouse P, Kellman P, Heslinga FG, Keenan K, Bruehl R, et al. A T1 and ECV phantom for global T1 mapping quality assurance: The T1 mapping and ECV standardisation in CMR (T1MES) program. J Cardiovasc Magn Reson [Internet]. 2016;18(1):W14. Available from: http://dx.doi.org/10.1186/1532-429X-18-S1-W14
43. Liu W, Turkbey B, Senegas J, Remmele S, Xu S, Kruecker J, et al. Accelerated T2 mapping for characterization of prostate cancer. Magn Reson Med. 2011;65(5):1400–6.

FIGURE LEGENDS

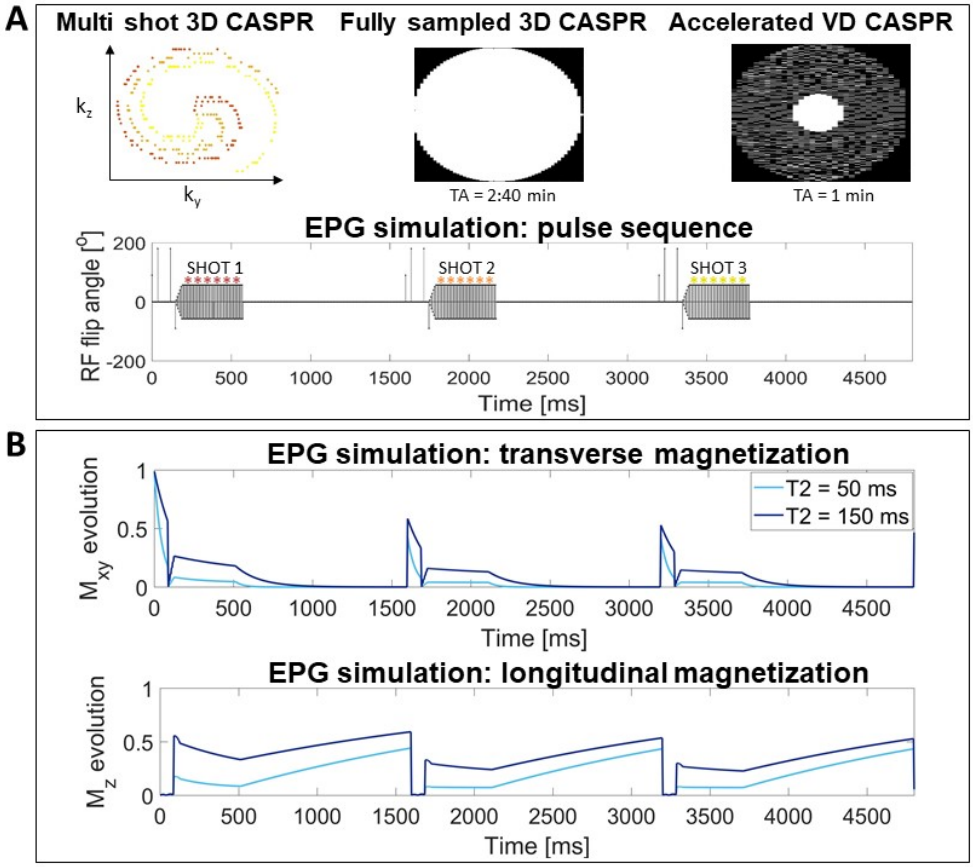

Figure 1: A) Multi shot 3D CASPR trajectory with fully sampled and variable density masks, shown together with three shots of the 3D multi-shot T_2prep-bSSFP pulse sequence. B) Corresponding transverse and longitudinal magnetization evolution obtained using the EPG simulation framework, for two different simulated T_2 values (50 and 150 ms). Other parameters of the simulation were: T_1 = 2200 ms, TR = 1600 ms, FA = 57°, T_2prep duration = 90 ms.

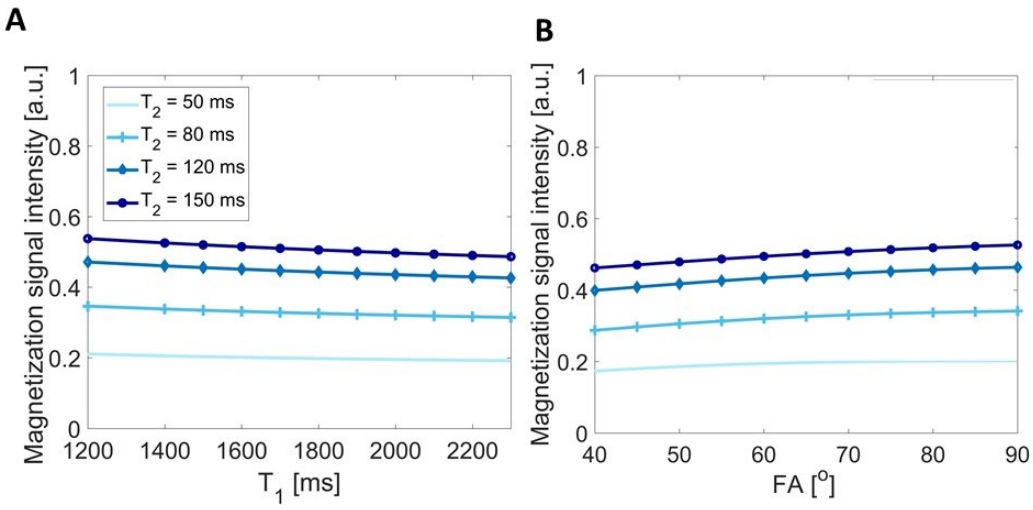

Figure 2: Insensitivity of the simulated signal intensity to T_1 variations typically observed in the prostate (A) and flip angle (FA) (B), for T_2 = 50, 80, 120, 150 ms.

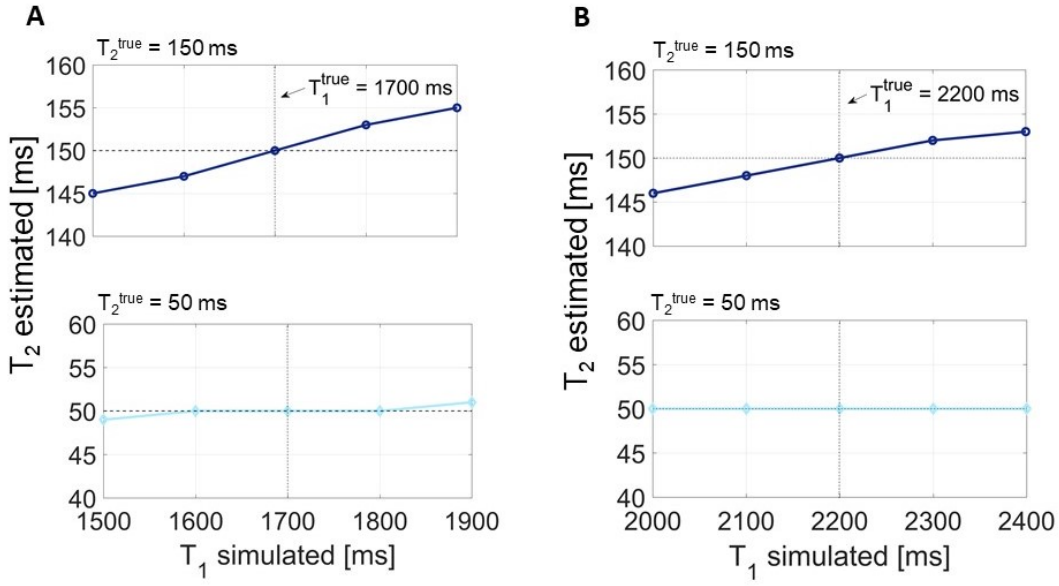

Figure 3: Simulation of the effect of using a T_1 value that differs from the T_1^{true} when using the proposed dictionary-based T_2 mapping method, for different simulated tissue types. A) T_1^{true} = 1700 ms, T_2^{true} = 50 and 150 ms. B) T_1^{true} = 2200 ms, T_2^{true} = 50 and 150 ms. The mapping seems to be very robust for low T_2 (50 ms), whereas higher T_2 (150 ms) values are slightly underestimated or overestimated when the simulated T_1 is respectively lower or higher than the T_1^{true}.

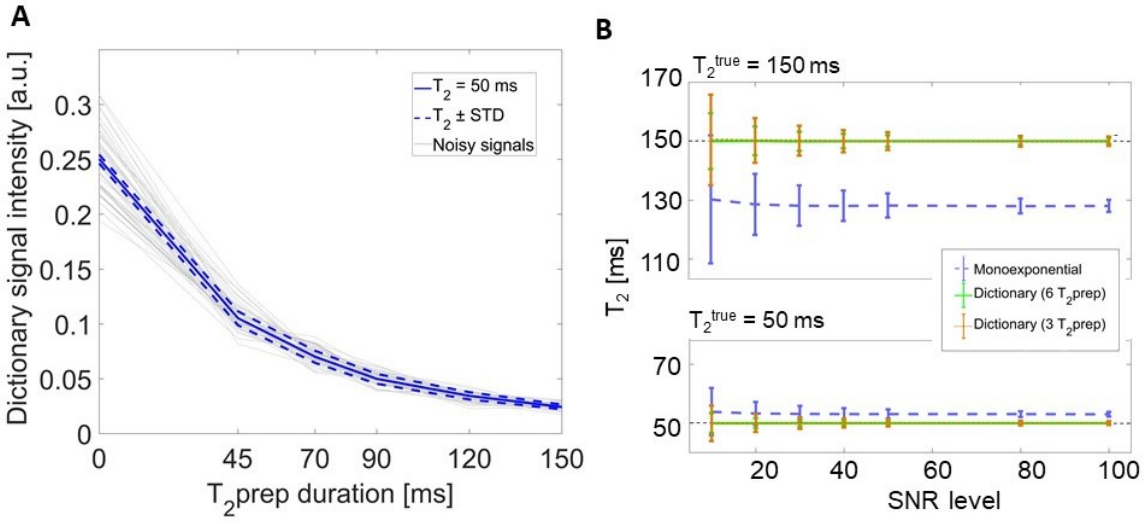

Figure 4: SNR analysis with different SNR levels, where accuracy and precision are calculated respectively as the mean ± standard deviation of the T_2 values estimated in the 5000 iterations of the Monte Carlo simulation. A) Dictionary entry with corresponding 100 noisy signals overlapped as an example case of SNR analysis for SNR = 10. B) Two different tissue types ($T_2^{low/high}$ = 50/150 ms, solid/dotted lines) are shown in the plot, for all three T_2 mapping methods: monoexponential fit and dictionary-based matching with six and three T_2prep durations. The monoexponential fit always led to a lower accuracy, showing a substantial bias, whereas with the dictionary-based matching the T_2 estimates improved and were comparable to the true simulated values.

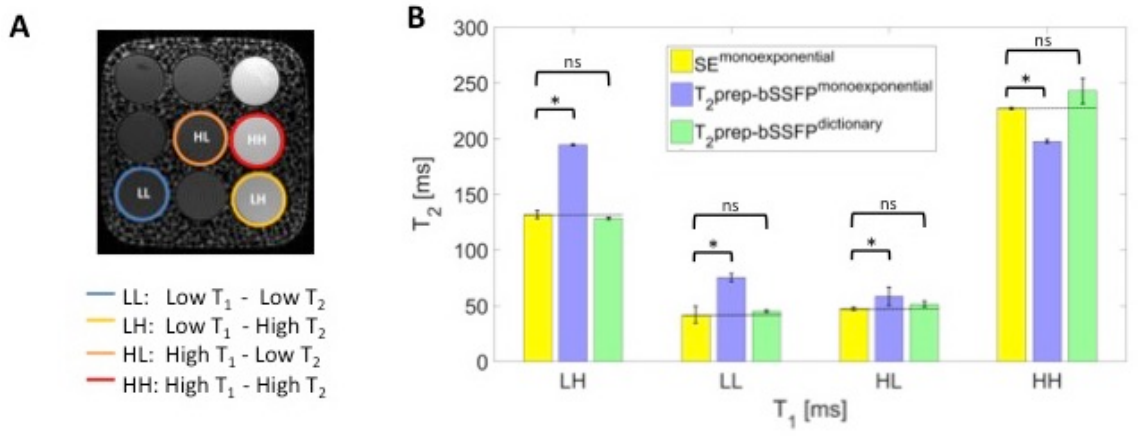

Figure 5: A) 2D SE T_2w image of the phantom; four tubes with different T_1 and T_2 combinations are highlighted in different colors. B) Comparison of T_2 values obtained in the phantom tubes highlighted in A with: gold standard 2D SE acquisition using monoexponential fit (yellow bar), fully sampled 3D T_2prep-bSSFP using both monoexponential fit (purple bar) and dictionary matching (green bar). Compared to gold standard, T_2 values obtained with the T_2prep-bSSFP using monoexponential fitting were significantly different ($P < 0.05$), whereas the acquisition-specific dictionary-based matching corrected for these inaccurate estimates.

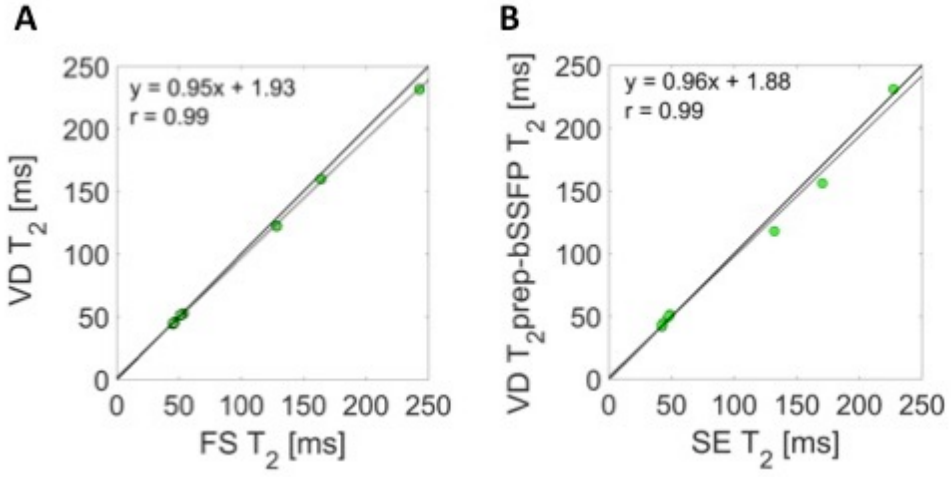

Figure 6: A) Correlation plot of T_2 values in all 9 phantom tubes obtained with FS and VD 3D T_2prep-bSSFP acquisitions, both obtained with the proposed dictionary matching approach, showing a correlation value r = 0.99. B) Correlation plot between gold standard 2D SE using monoexponential fit (TA = 1 h 55 min 51 s) and proposed rapid method (VD 3D T_2prep-bSSFP with dictionary matching using three T_2prep/data points, TA = 3 min), with correlation value r = 0.99.

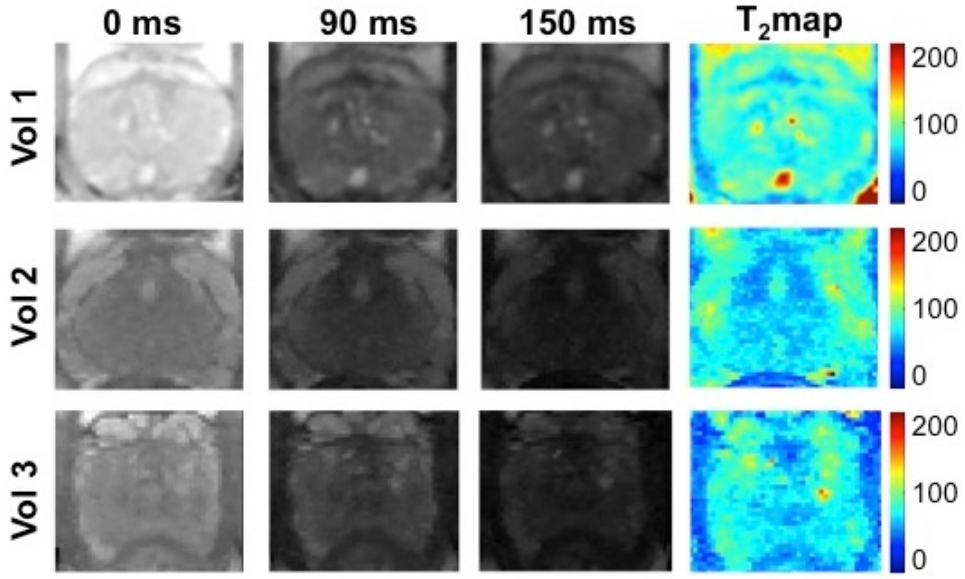

Figure 7: T_2w prostate images obtained with VD 3D T_2prep-bSSFP and three different T_2prep durations (0, 90, 150 ms), and correspondent T_2map obtained with the proposed dictionary-based T_2 mapping, for three healthy subjects part of our feasibility study.

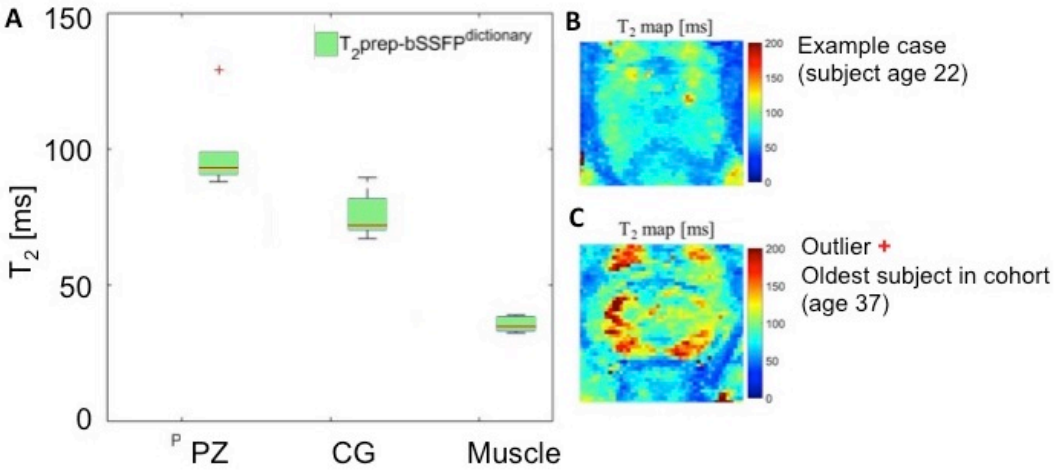

Figure 8: A) T_2 values of peripheral zone (PZ), central gland (CG) and muscle in the healthy subjects obtained with the proposed VD 3D T_2prep-bSSFP sequence and dictionary-based T_2 mapping. Example cases of a T_2 map of a young subject (B) and of the oldest subject in the cohort (C), which is the only outlier (+) with higher (comparable to literature) T_2.

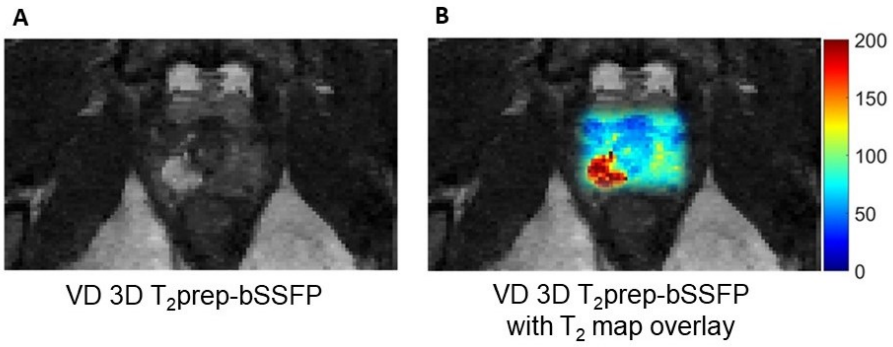

Figure 9: Example case of a healthy subject with focal inflammation found in the peripheral zone (PZ). A) 3D VD T_2w T_2prep-bSSFP (T_2prep = 90 ms) with T_2 map overlay (B). Estimated T_2 values with the proposed 3D VD T_2prep-bSSFP using dictionary matching are T_2 = 89 ± 16.1 ms in the normal PZ and 187.8 ± 26.4 ms in the inflammation area.

SUPPLEMENTARY FIGURE LEGENDS

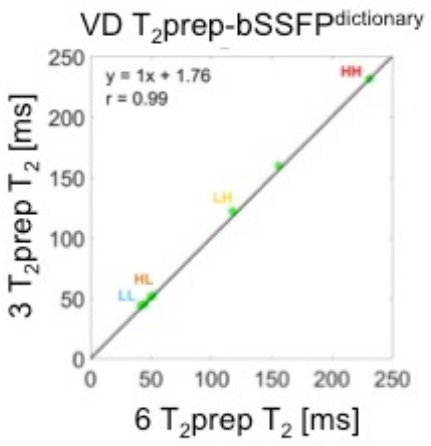

Supplementary Figure 1: D) Correlation plot of T_2 values obtained in the phantom with VD 3D T_2prep-bSSFP acquisition with dictionary matching using six T_2prep and three T_2prep, showing high correlation (r = 0.99). The scan time is reduced from TA = 6 min to 3 min when using only three T_2prep.

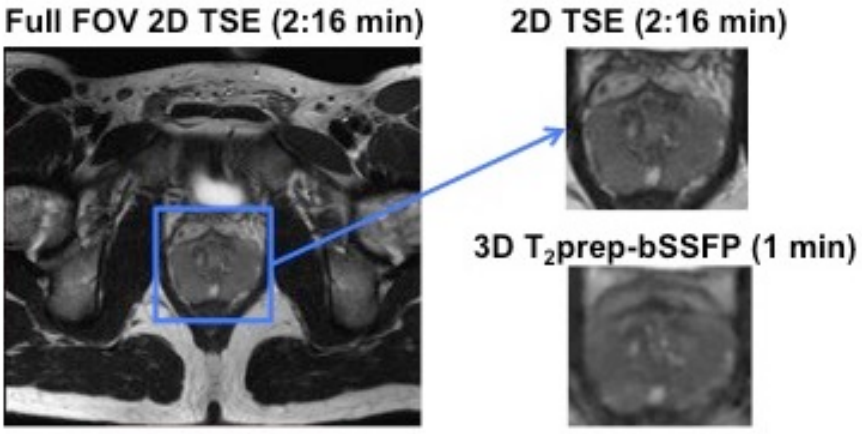

Supplementary Figure 2: Full field of view (FOV) of the reference clinical standard 2D T_2w TSE acquisition (resolution 0.6 x 0.8 x 3 mm^3, TE = 89 ms) with detail of the prostate, together with the VD 3D T_2w T_2prep-bSSFP image (resolution 0.9 x 0.9 x 3 mm^3, T_2prep duration 90 ms).

ACKNOWLEDGEMENTS

This work is funded by the King's College London & Imperial College London EPSRC Centre for Doctoral Training in Medical Imaging (EP/L015226/1) and was supported by the Wellcome EPSRC Centre for Medical Engineering at King's College London (WT 203148/Z/16/Z). We acknowledge funding from The King's Health Partners Research and Development Challenge Fund, TOHETI, NIHR BRC, GSTT/KCL BRC, CRUK/EPSRC Cancer Centre, and Siemens Healthineers.